A study of the fine scale motions of incompressible time-developing mixing layers

By J. Soria[1], M. S. Chong[2], R. Sondergaard[3], A. E. Perry[4] AND B. J. Cantwell[3]

This work is an extension of a project conducted at the previous CTR summer program and was reported by Chen *et al.* (1990). In that program, the geometry and topology of the dissipating motions in a variety of shear flows was examined. All data was produced by direct numerical simulations (DNS). The partial derivatives of the velocity field were determined at every grid point in the flow and various invariants and related quantities were computed from the velocity gradient tensor. Motions characterized by high rates of kinetic energy dissipation and high enstrophy were of particular interest. Scatter diagrams of the invariants were mapped out and interesting and unexpected patterns were seen. Each type of shear layer produced its own characteristic scatter plot.

In the present project, attention is focused on the incompressible plane mixing layer, and the scatter diagrams are replaced with more useful joint probability density contours. Comparison of the topology of the dissipating motions of flows at different Reynolds numbers are made. Also, plane mixing layers at the same Reynolds number but with different initial conditions are compared.

1. Method of approach

The velocity gradient tensor may be broken up into a symmetric and an antisymmetric part $A_{ij} = \partial u_i/\partial x_j = S_{ij} + W_{ij}$ where $S_{ij} = (\partial u_i/\partial x_j + \partial u_j/\partial x_i)/2$ and $W_{ij} = (\partial u_i/\partial x_j - \partial u_j/\partial x_i)/2$ are the rate-of-strain and rate-of-rotation tensors, respectively. The eigenvalues of A_{ij} satisfy the characteristic equation

$$\lambda^3 + P\lambda^2 + Q\lambda + R = 0 \tag{1}$$

where the matrix invariants are:

$$P = -(A_{11} + A_{22} + A_{33}) = -\text{trace}[A] = -S_{ii} \tag{2}$$

1 C.S.I.R.O., Highett, Australia.
2 Dept. of Mechanical Engineering, University of Melbourne, Australia.
3 Department of Aeronautics and Astronautics, Stanford University
4 Currently GALCIT, California Institute of Technology.

$$Q = \begin{vmatrix} A_{11} & A_{12} \\ A_{21} & A_{22} \end{vmatrix} + \begin{vmatrix} A_{11} & A_{13} \\ A_{31} & A_{33} \end{vmatrix} + \begin{vmatrix} A_{22} & A_{23} \\ A_{32} & a_{33} \end{vmatrix}$$
$$= \frac{1}{2}\left[P^2 - \text{trace}[A^2]\right] \tag{3}$$
$$= \frac{1}{2}[P^2 - S_{ij}S_{ji} - W_{ij}W_{ji}]$$

and

$$R = -\begin{vmatrix} A_{11} & A_{12} & A_{13} \\ A_{21} & A_{22} & A_{23} \\ A_{31} & A_{32} & a_{33} \end{vmatrix} = -\det[A]$$
$$= \frac{1}{3}(-P^3 + 3PQ - \text{trace}[A^3]) \tag{4}$$
$$= \frac{1}{3}(-P^3 + 3PQ - S_{ij}S_{jk}S_{ki} - 3W_{ij}W_{jk}S_{ki}).$$

It can be shown that, in the $P - Q - R$ space of matrix invariants, the surface which divides characteristic equations with three real solutions for the eigenvalues from characteristic equations with one real and two complex solutions is

$$27R^2 + (4P^3 - 18PQ)R + (4Q^3 - P^2Q^2) = 0. \tag{5}$$

A detailed discussion of the properties of this surface is given in Chong, Perry & Cantwell (1990) along with a guide to the various possible elementary flow patterns which can occur in different domains.

Much of the discussion in this report concerns the symmetric part of the velocity gradient tensor, the second invariant of which is proportional to the negative of the kinetic energy dissipation. The invariants of the rate-of-strain tensor, P_S, Q_S and R_S, are generated by setting the components of W_{ij} to zero in the above relations. The flows considered are, with one exception, incompressible hence $P = P_S = 0$. Thus the local geometry of the flow is completely described by the second and third invariants (Q, R) and (Q_S, R_S). The second invariant of the rate-of-rotation tensor, Q_W, is non-zero and is proportional to the enstrophy. The first and third invariants of the rate-of-rotation tensor are identically zero.

The method for classifying the flow structure was first developed at the 1990 CTR summer program by Chen *et al.* (1990) and is described as follows:

(i) Evaluate the nine partial derivatives of the velocity gradient tensor at every point in the computed field.

(ii) Evaluate Q, R, Q_S, R_S and Q_W at every point.

(iii) Create scatter plots of the results in the space of invariants, Q versus R, Q_S versus R_S , and $-Q_S$ versus Q_W.

Figure 1 illustrates the various flow topologies which can occur in the plane $P = 0$. The intersection of this plane with the surface (5) is given by

$$R = \pm\frac{2\sqrt{3}}{9}(-Q)^{3/2} \tag{6}$$

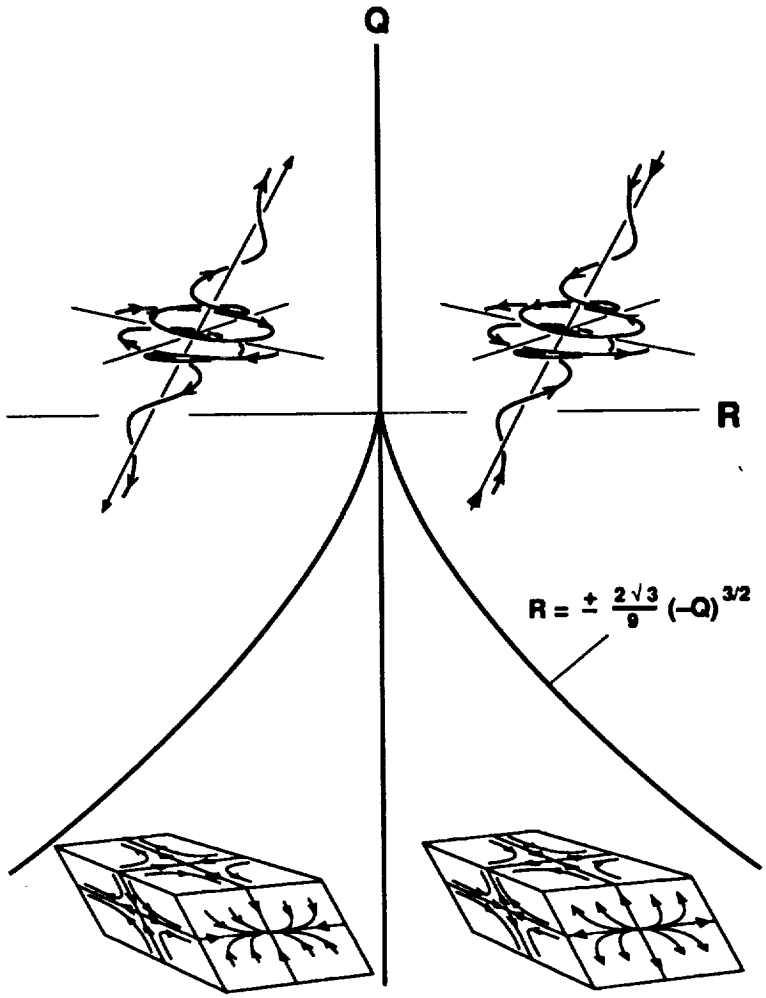

FIGURE 1. Three-dimensional topologies in the $Q - R$ ($P = 0$) plane.

which divides real solutions from complex solutions as indicated.

For the case $P = 0$, the second invariant is

$$Q = \frac{1}{2}[W_{ij}W_{ij} - S_{ij}S_{ij}] \tag{7}$$

where the indices have been switched to indicate explicitly that Q is formed from the difference of two terms, each of which is a positive sum of squares. The local topology has complex or real eigenvalues depending on whether the (Q, R) pair evaluated at a given point in the flow lies above or below (6).

The mechanical dissipation of kinetic energy due to viscous friction is

$$\phi = 2\nu S_{ij}S_{ij} = -4\nu Q_S. \tag{8}$$

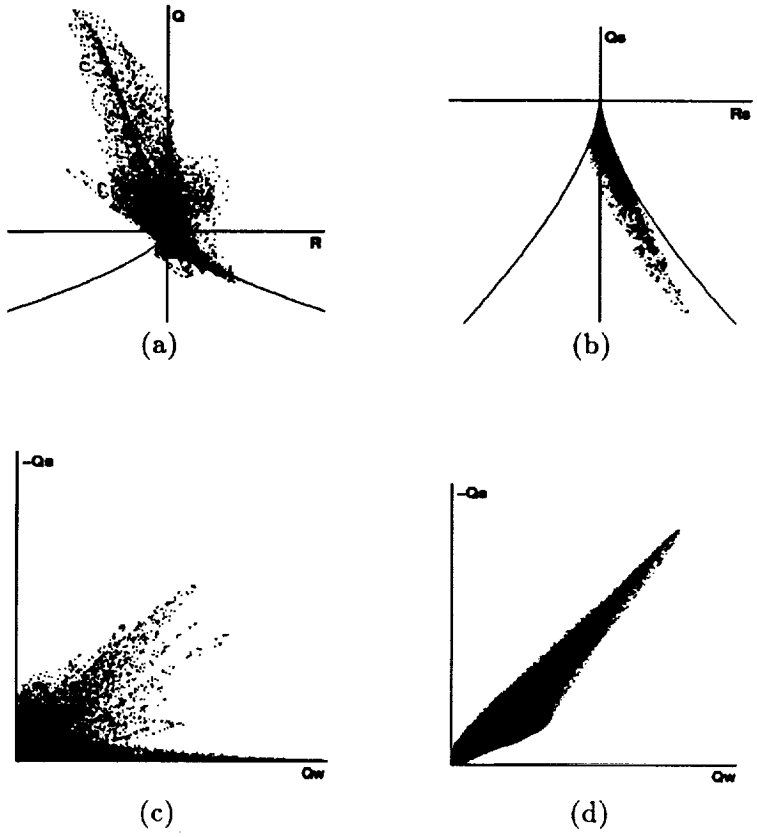

FIGURE 2. Scatter plots of (a) Q vs. R, (b) Q_s vs. R_s, (c) $-Q_s$ vs. Q_w for *hipairex* at $tU/\delta_0 = 29.8$, and (d) Q_s vs. Q_w for a compressible mixing layer computed by Chen (1991) at $tU/\delta_0 = 72.0$.

Large negative values of Q_S correspond to large rates of dissipation of kinetic energy. Large negative values of Q indicate regions where the strain is both large and strongly dominant over the enstrophy. Large positive values of Q indicate the reverse.

2. Results

We will consider in this paper the incompressible ($P = 0$) plane mixing layers computed by Rogers and Moser at NASA Ames. Three direct numerical simulations (DNS) are considered, namely, *hipairex*, *mega*, and *tbl*. The cases *hipairex* and *mega* were initiated from laminar error function profiles, and *tbl* was initiated with two turbulent boundary layer realizations with equal and opposite free stream velocities placed on opposite sides of a dividing plate which was dissolved at time $t = 0$. The initial turbulent boundary layers were DNS computations of Spalart (1988).

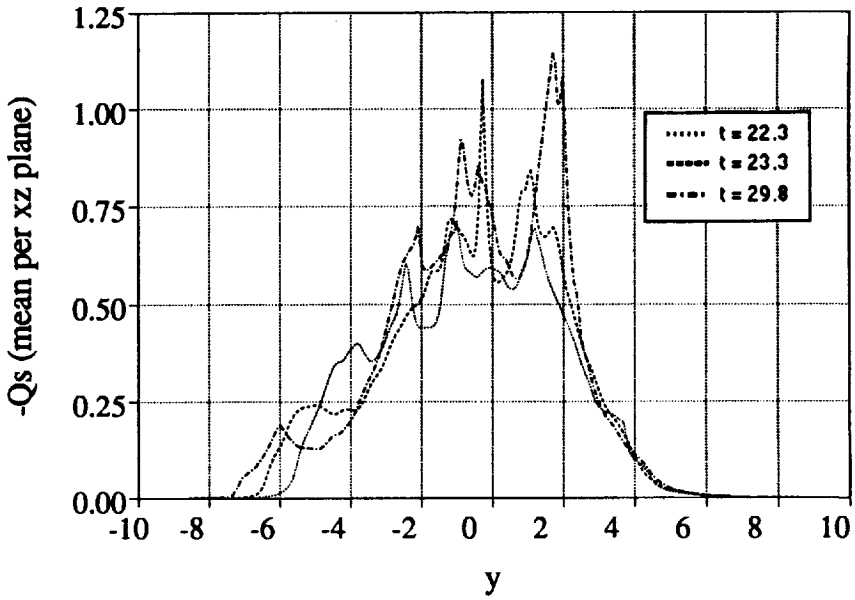

FIGURE 3. Planar x-z average $\overline{Q_s}$ vs. cross-stream direction y for *hipairex* at $tU/\delta_0 = 22.3, 25.3, 29.8$.

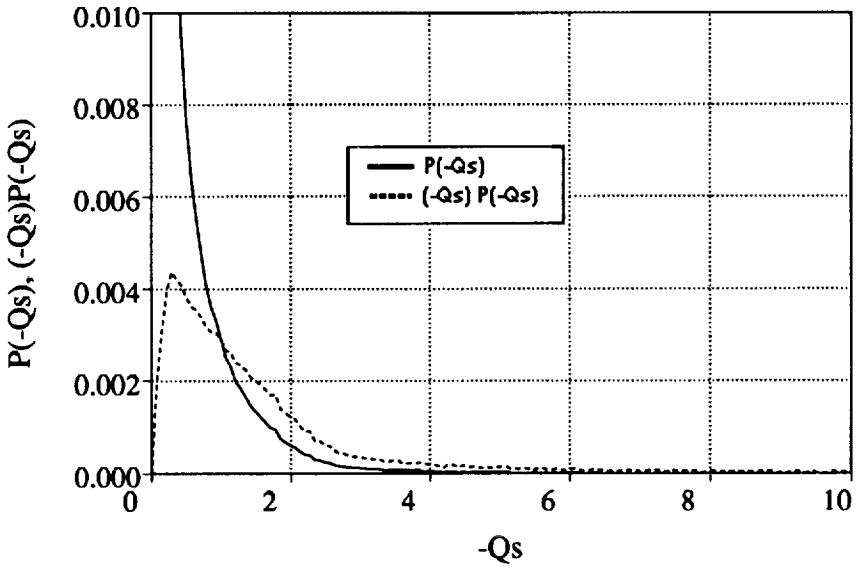

FIGURE 4. Weighted Probability Density Functions $P(-Q_s)$ and $(-Q_s)P(-Q_s)$ vs. $-Q_s$ for *hipairex* at at $tU/\delta_0 = 29.8$.

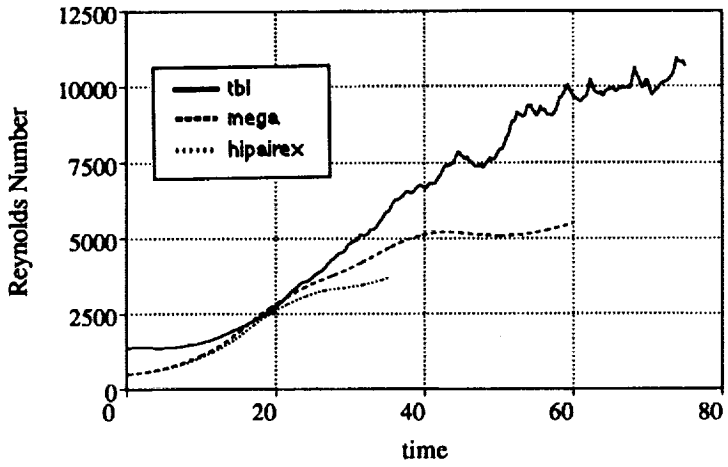

FIGURE 5. Vorticity thickness Reynolds number R_δ vs. non-dimensional time for the incompressible mixing layers.

Table I

	hipairex	*mega*	*tbl*
$\Delta U = U_2 - U_1$	2	2	2
Initial vorticity thickness, δ_0	1	1	1.4
Viscosity, ν	1/250	1/250	1/500
Initial $Re = \Delta U \delta_0 / 2\nu$	250	250	700

All cases were computed as time developing layers and Table I shows the properties of the layers. Details of the *hipairex* results have been reported by Moser & Rogers (1990) and Rogers & Moser (1992). Unless otherwise stated, all results are normalized by half the velocity difference across the layer, U, and the initial vorticity thickness δ_0. Figures 2(a), 2(b) and 2(c) show scatter diagrams taken from Chen *et al.* (1990). These diagrams are made up of the entire data set for a given time. Figure 2(a) shows that most of the high gradient motions belong to the topology of stable focus stretching. Figure 2(c) is most informative. Data which falls on the line of 45° through the origin represents high dissipation accompanied by high enstrophy. It can be shown that such points come from vortex sheets where most of the rate-of-strain is dominated by the velocity gradient within the sheet. Data which lies along the horizontal axis represents high enstrophy with little dissipation as would occur in solid body rotation in vortex tubes. As a matter of interest, Figure 2(d) shows a plot from a compressible mixing layer computation by Chen (1990), and, according to the figure, the data could be described as primarily sheet-like. The reason for this is a mystery at this stage.

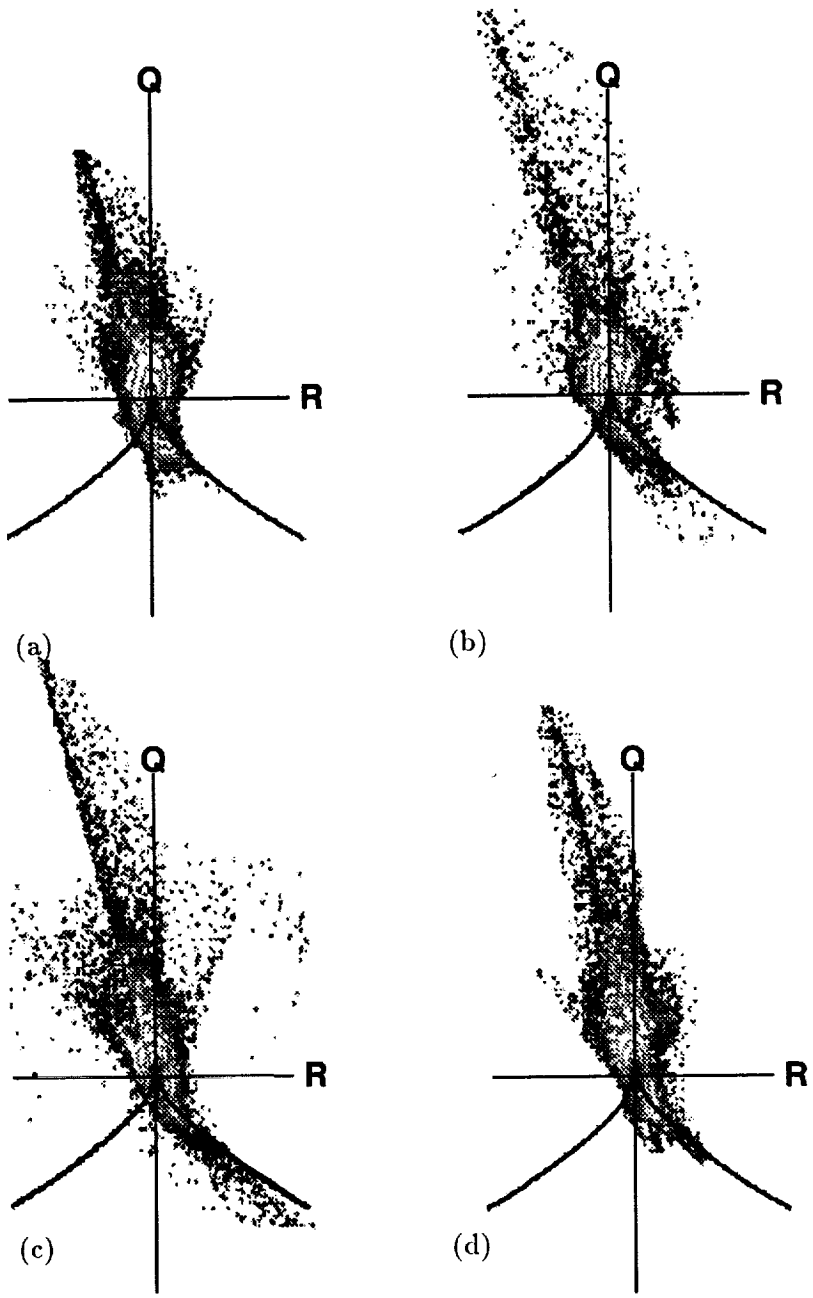

FIGURE 6. Q vs R for *hipairex*. tU/δ = (a) 19.3, (b) 22.3, (c) 25.3, (d) 29.8.

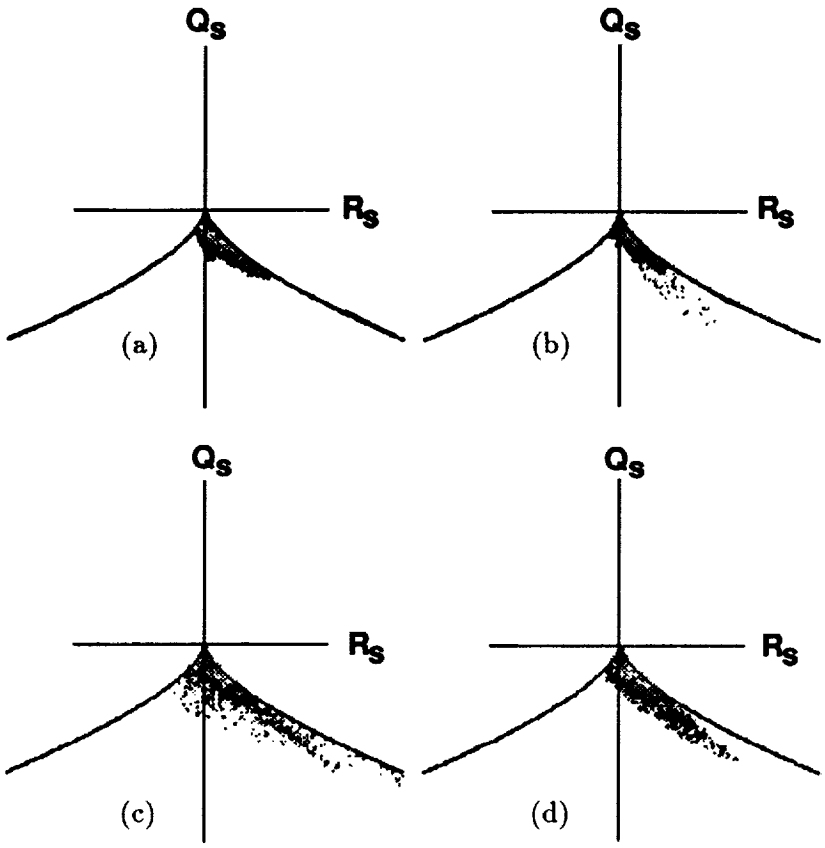

FIGURE 7. Q_s vs R_s for *hipairex*. tU/δ = (a) 19.3, (b) 22.3, (c) 25.3, (d) 29.8.

Classical arguments, based on the idea that dissipation of turbulent kinetic energy scales with production, lead to the following estimates:

$$\epsilon = 2\nu\overline{S'_{ij}S'_{ij}} = -\overline{u'v'}\frac{\partial\overline{U}}{\partial y} \tag{9}$$

where the S'_{ij} are fluctuating non-normalized strain rates. Results from experiment show that for fully developed shear layers

$$-\overline{u'v'}/(\Delta U)^2 \simeq .012 = \frac{-\overline{u'v'}}{4U^2}. \tag{10}$$

From (9) and (10) it can be shown that

$$\epsilon = 2\nu\overline{S'_{ij}S'_{ij}} = .096U^3/\delta \tag{11}$$

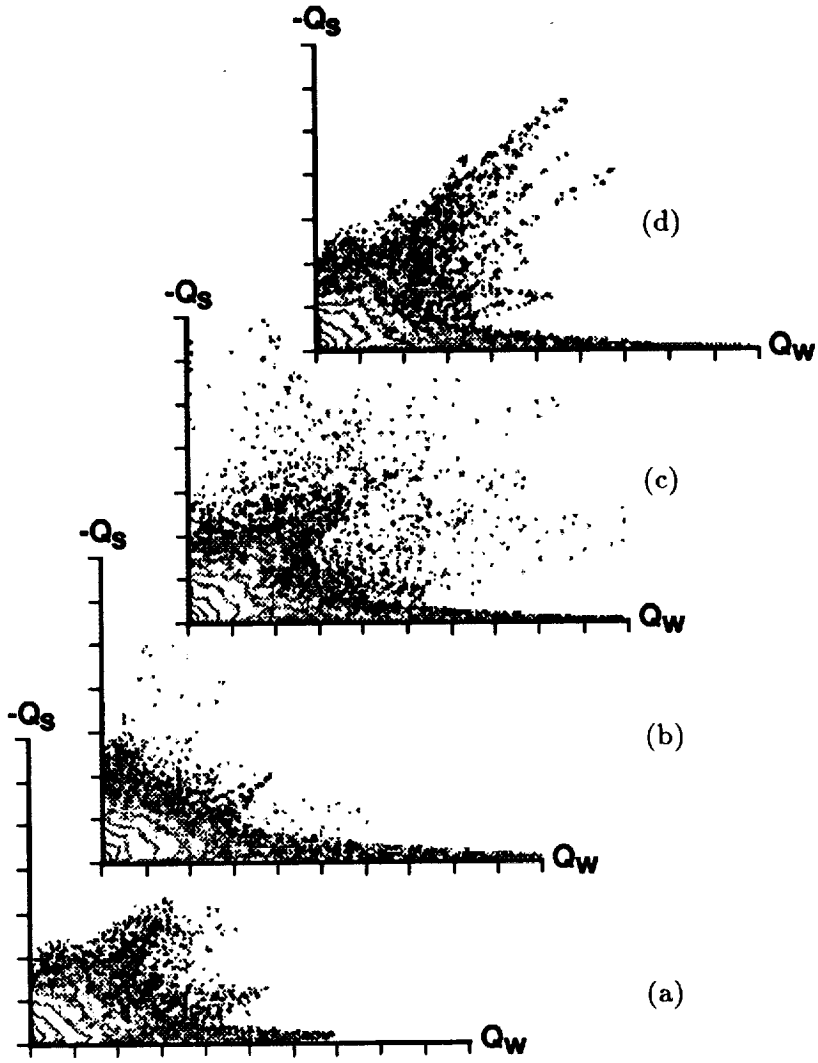

FIGURE 8. $-Q_s$ vs Q_w for *hipairex*. tU/δ = (a) 19.3, (b) 22.3, (c) 25.3, (d) 29.8.

For time $tU/\delta_0 = 29.8$ in *hipairex* where the vorticity thickness has increased by a factor of 6.5 over the initial thickness, the Reynolds number R_δ based on the current vorticity thickness, δ, and the velocity difference across the layer is 3000. Hence

$$\frac{\overline{S'_{ij}S'_{ij}}\delta_0^2}{U^2} \simeq \frac{.096}{4} R_\delta \left(\frac{\delta_0}{\delta}\right)^2 = 1.704. \tag{12}$$

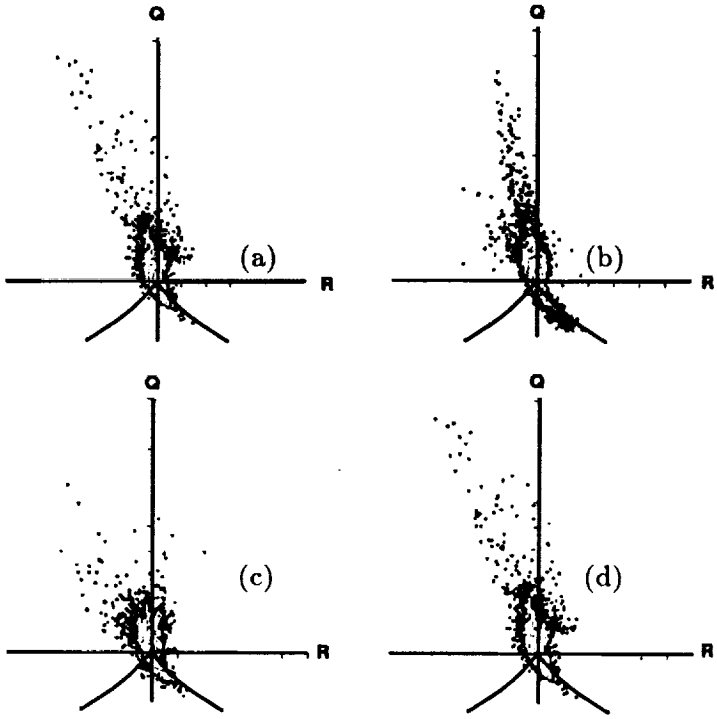

FIGURE 9. Q vs R for *mega*. tU/δ = (a) 21.0, (b) 25.0, (c) 35.0, (d) 49.0.

One would expect the average value of this quantity at the midplane of the mixing layer to be of this order.

Mean profiles of $-Q_S$ at various times are shown in Figure 3 and are half the value indicated by (12) which is indicative of the production of kinetic energy. This ratio of about 2 for production to dissipation is in agreement with the fully developed value obtained from experiments by Bradshaw & Ferriss (1967). An order of magnitude analysis similar to (12) reported by Chen *et al.* (1990) giving the value of 18.2 was in error due to incorrect normalization of the variables.

Figure 4 shows the weighted probability density function of $-Q_S$ over the entire volume of the mixing layer, and most of the contribution comes from $-Q_S$ between 0 and 3. Although the far flung values of $-Q_S$ on the scatter diagram tend to follow interesting patterns, they contribute only of order 10% to the total energy dissipation. For this reason, it was felt that scatter diagrams should be replaced by joint probability density diagrams with contours corresponding to the logarithm of the probability density function so that possible ridges could be seen in regions which are highly darkened in the scatter plots.

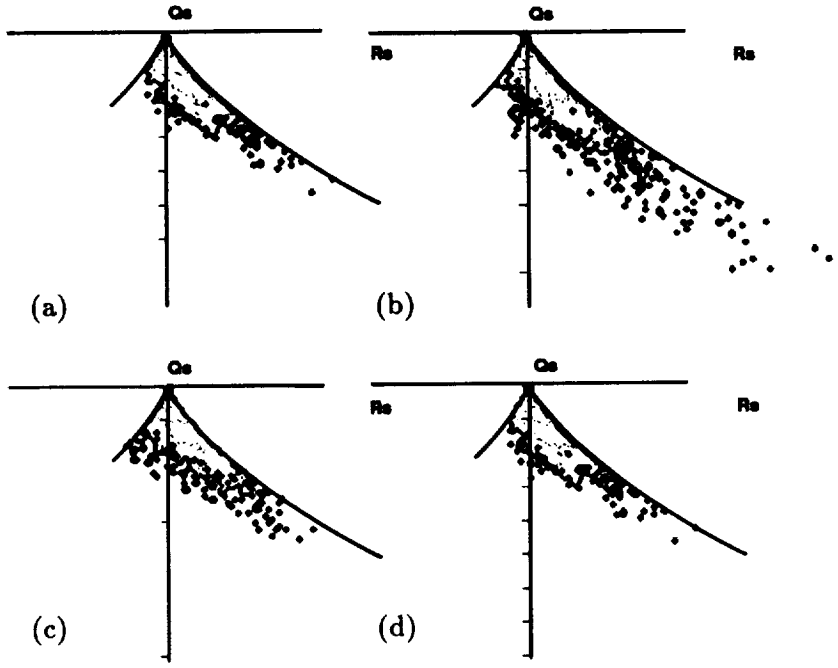

FIGURE 10. Q_s vs R_s for *mega*. tU/δ = (a) 21.0, (b) 25.0, (c) 35.0, (d) 49.0.

From (11) and (12) it can be seen that Q_S normalized by the current vorticity thickness scales with R_δ, and, therefore, it seems likely that R_S should scale with $R_\delta^{3/2}$. This would imply that the data should follow a curve

$$|R_s| \propto (|Q_s|)^{\frac{3}{2}} \tag{13}$$

This relationship is what one might expect purely on dimensional grounds, but there is no rigorous proof. It is interesting to note that such a curve on the Q_S versus R_S plot represents a rate of strain geometry where the principal rates of strain α, β and γ are in a constant ratio to one another. For the data set *hipairex*, points of high dissipation follow closely the curve corresponding to the ratio of $\alpha:\beta:\gamma = 3 : 1 : -4$, which was observed by Ashurst *et al.* (1987) in studies of forced isotropic turbulence. In addition, as noted by Sondergaard *et al.* (1991), the vorticity vector tends to align itself with the second principle rate of strain β. It should be noted that while other data sets analyzed by Sondergaard *et al.* (1991) show the same vorticity alignment, the 3:1:−4 ratio of rates of strain is not always observed.

The result depicted in 2(b) is that motions characterized by very high rates of dissipation (large negative Q_S) clearly show a preference for the right half plane of Figure 2(b) corresponding to a local topology of the rate of strain tensor which is

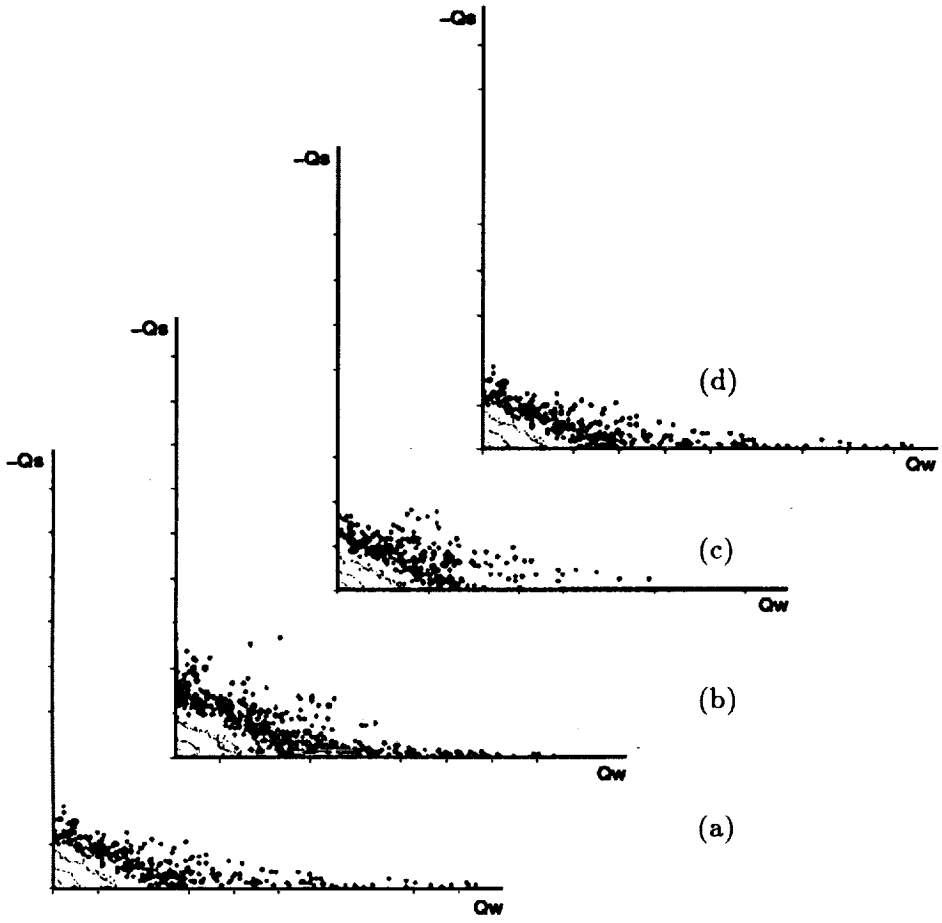

FIGURE 11. $-Q_s$ vs Q_w for *mega*. tU/δ = (a) 21.0, (b) 25.0, (c) 35.0, (d) 49.0.

of the type saddle-saddle-unstable node (cf. Figure 1). From Figure 2(a), it can be seen that the velocity gradient tensor admits all possible incompressible topologies although there is, nevertheless, a great deal of structure in Figure 2(a). Not only is the basic scaling (12) observed, but it appears that, with a modest amount of scatter, the fine scale motions follow a relation of the form

$$R_s \cong K(-Q_s)^{\frac{3}{2}}. \tag{13}$$

The positive quantity K is expected to be a function of the Reynolds number with an upper limit of $K = 2\sqrt{3}/9$ corresponding to locally axisymmetric flow (cf. Figure 1).

3. Comparison with high Reynolds number flows

Figure 5 shows a plot of Reynolds number based on current vorticity thickness for the three cases mentioned earlier. Figures 6, 7, and 8 show the invariant plots

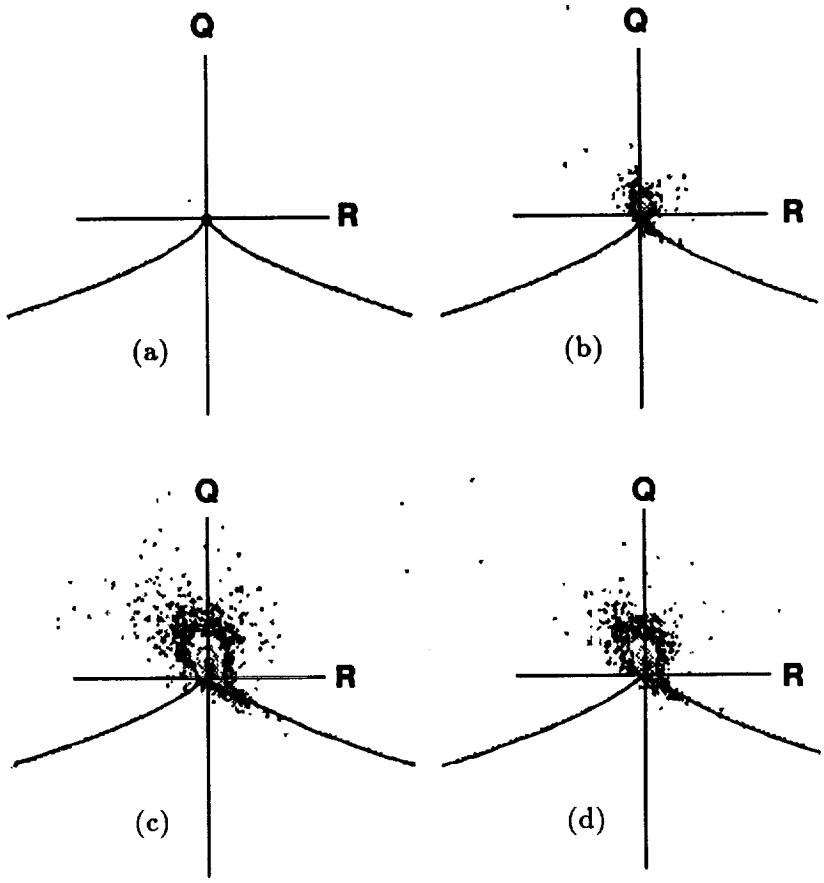

FIGURE 12. Q vs R for *tbl.* tU/δ = (a) 0.0, (b) 26.25, (c) 47.5, (d) 76.25.

for *hipairex* in contour plot form for the joint probability density distributions. Figures 9, 10, and 11 show the results for *mega*. These results are similar to the scatter diagrams given in Figure 2 but are corrected for nonuniform grid spacing. More structural features are apparent, and an interesting feature in Figures 6 to 8 is that velocity gradients tend to increase with time and at the latest time show a decrease. In fully developed turbulent plane mixing layers, if dissipation scales with production, then according to the Kolmogorov scaling, the velocity gradients should decrease with time. According to this reasoning, *hipairex* is under-developed for most if not all of the times shown. It is unclear whether, at the latest time, the gradients are beginning to decrease because the flow is reaching a fully developed state or because of constraining by the grid. Figures 9, 10, and 11 show the results for *mega*, and there appears less pronounced sheet-like structures but more tube-like patterns for the higher Reynolds numbers.

Figures 12, 13, and 14 show similar results for *tbl.* which started out as two

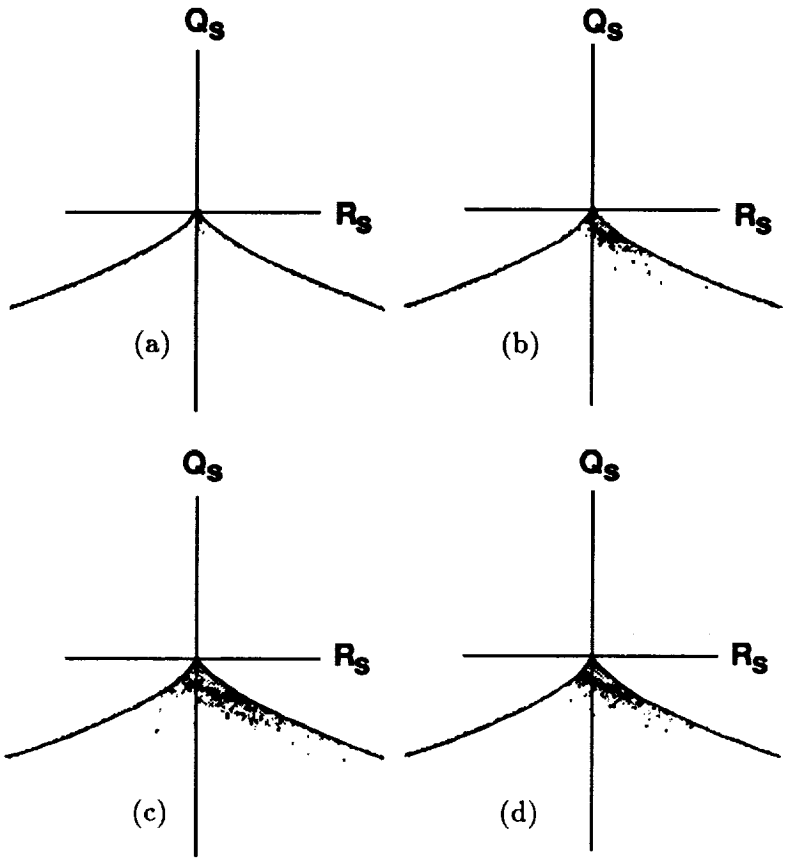

FIGURE 13. Q_s vs R_s for *tbl.* tU/δ = (a) 0.0, (b) 26.25, (c) 47.5, (d) 76.25.

turbulent boundary layers and then developed to a much higher Reynolds number than *hipairex*. Figure 12 is most interesting. It shows that all data points for the turbulent boundary layer cluster near the origin of the Q versus R plot and suddenly explode to much higher gradients in the plane mixing layer. These pictures graphically illustrate how much greater velocity gradients become when the wall constraint of a turbulent boundary layer is removed. It should be noted that near the wall, the Q and R of a turbulent boundary layer are small even when the gradients aren't. A better measure of the relative magnitudes of the velocity gradients can be inferred from figure 14. Again, the gradients tend to grow and then diminish at late times. The Q_S versus R_S plot shows that the strain rates tend to follow a different curve, closer to the real-imaginary dividing surface (6). Hence, this aspect of the fine scale motion appears to be Reynolds number dependent. The plots in Figure 14 show that the turbulent boundary layer structures at $t' = 0$ are sheet-like, but, in contrast to *hipairex*, there are no preferred structures revealed by the $-Q_S$ versus Q_W plot for later times (cf. Figure 8). As with *hipairex* the Q versus R plot

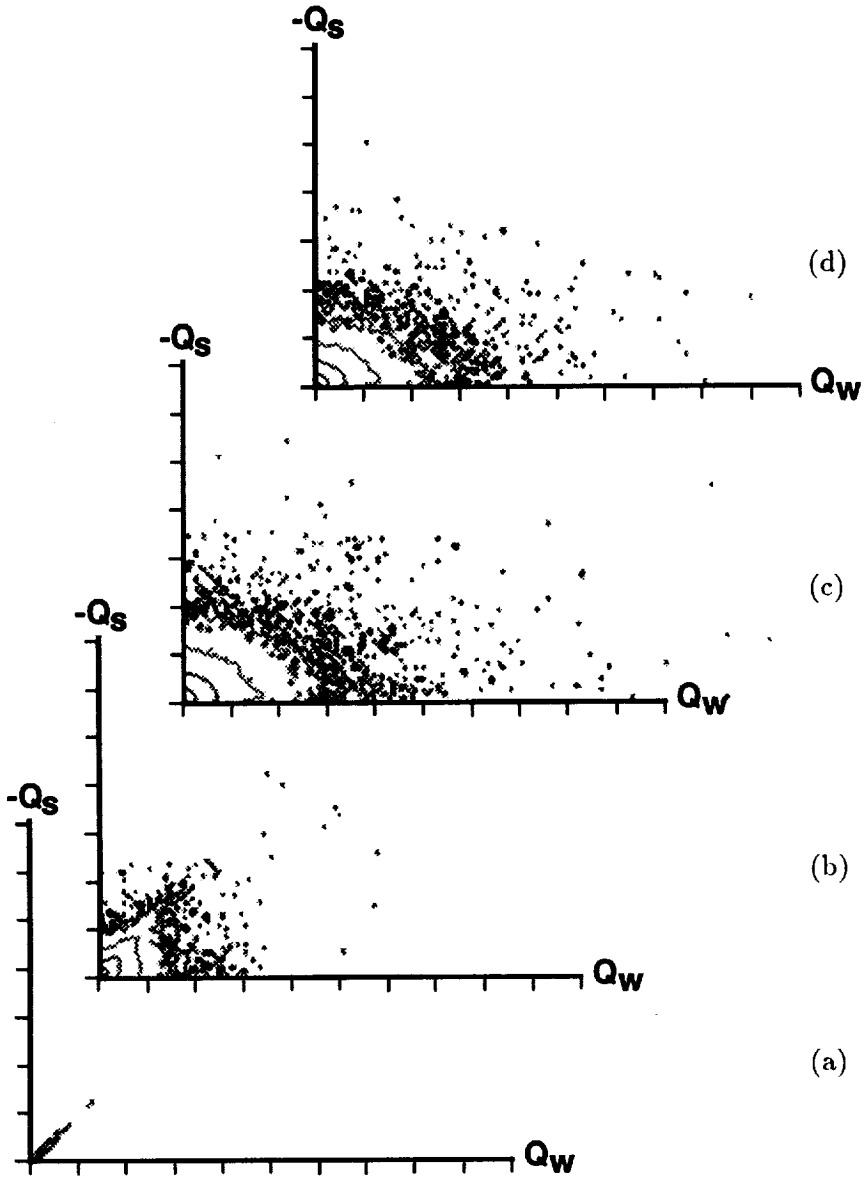

FIGURE 14. $-Q_s$ vs Q_w for *tbl.* tU/δ = (a) 0.0, (b) 26.25, (c) 47.5, (d) 76.25.

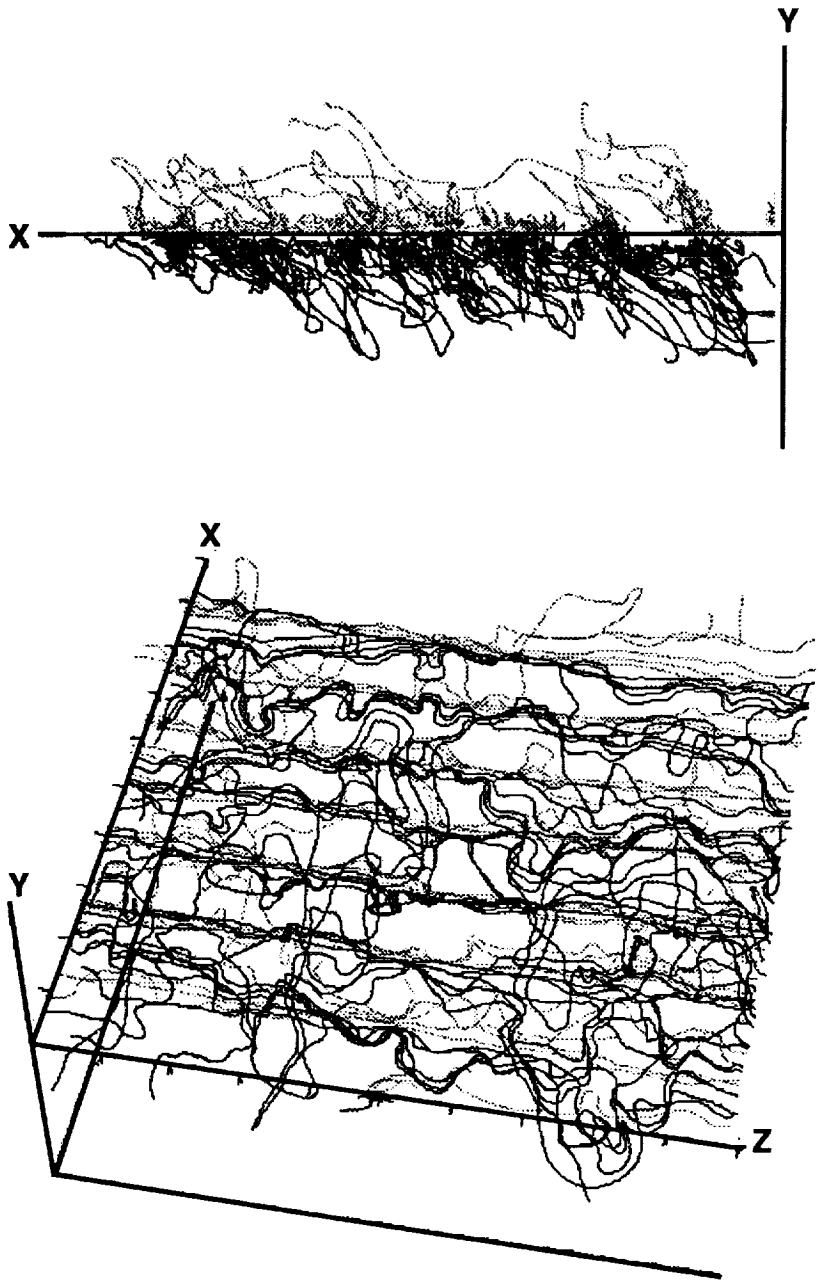

FIGURE 15. Vortex lines for *tbl* at $tU/\delta = 0.0$.

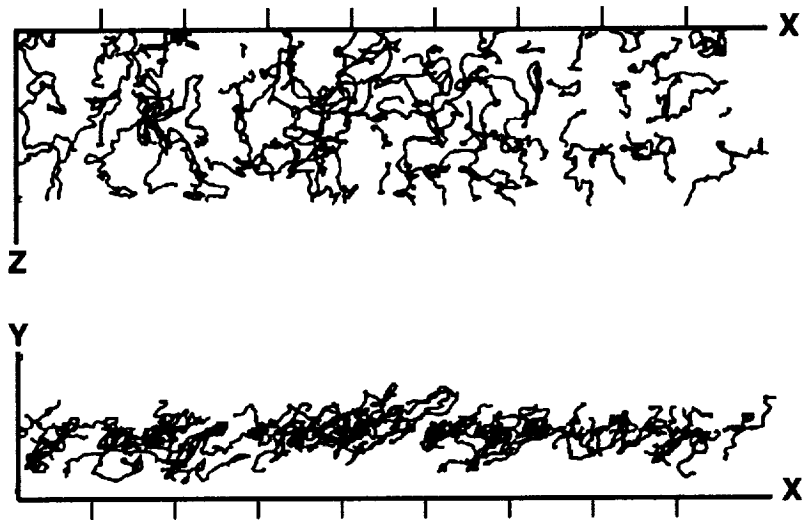

FIGURE 16. Vortex lines for *tbl* at $tU/\delta = 76.3$.

FIGURE 17. Streamlines for *tbl* at $tU/\delta = 76.3$.

shows that most of the gradients belong to the topology of stable focus stretching.

The highly organized patterns seen in Chen *et al.* (1990) for *hipairex* are replaced by most complex structures in *tbl*. Vortex lines for *tbl* are shown in Figures 15 and 16. Shown in Figure 15 is the initial turbulent boundary layer, and the attached eddies which lean approximately 45° to the mean flow direction are apparent. In Figure 16 are shown vortex lines of the plane mixing layer after some development. Although no clear spanwise rollups are apparent from this vorticity plot, Figure 17 shows instantaneous streamline patterns which indicate possible large scale spanwise roll-ups.

4. Comparison of two initial conditions at the same Reynolds number

From Figure 5, it can be seen that there is an overlap of Reynolds numbers for *mega* and *tbl*. In fact, they both share a Reynolds number of 5000 as indicated in the

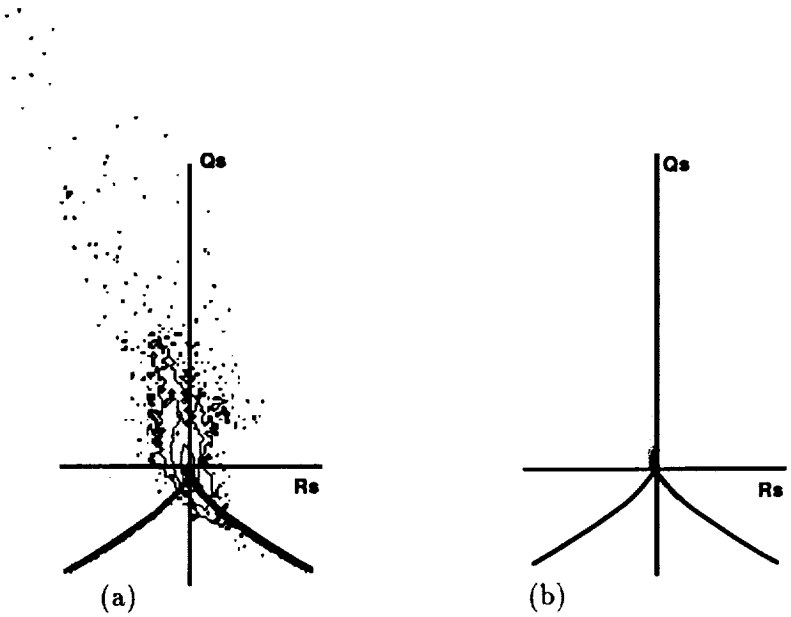

FIGURE 18. Rescaled Q vs. R plots for (a) *mega* at $tU/\delta = 49.0$, (b) *tbl* at $tU/\delta = 61.0$.

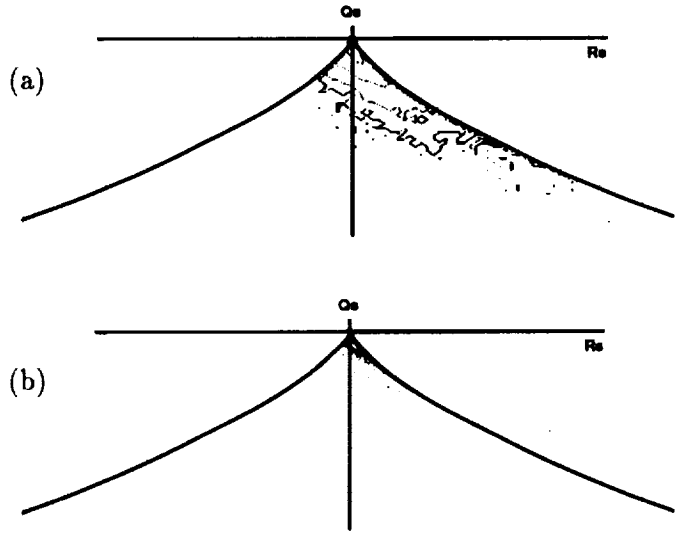

FIGURE 19. Rescaled Q_s vs. R_s plots for (a) *mega* at $tU/\delta = 49.0$, (b) *tbl* at $tU/\delta = 61.0$.

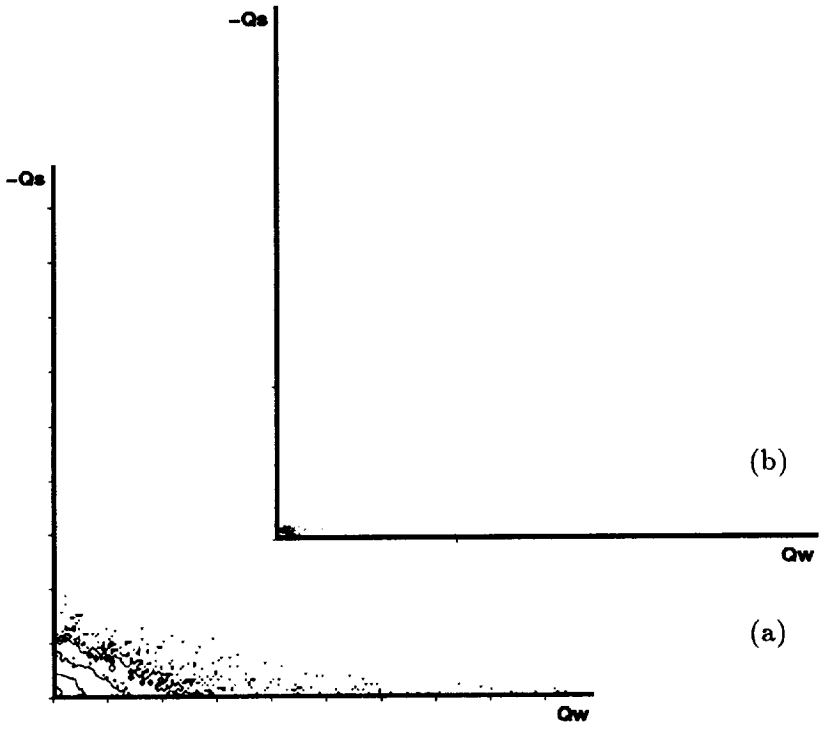

FIGURE 20. Rescaled $-Q_s$ vs. Q_w plots for (a) *mega* at $tU/\delta = 49.0$, (b) *tbl* at $tU/\delta = 61.0$.

figure. Figures 18(a) and (b) show Q versus R plots of *tbl* and *mega*, each scaled with the current vorticity thickness and appropriate velocity U. The joint probability density contours have been rescaled to account for the different population density of points. Figures 19 (a) and (b) show the corresponding $-Q_S$ versus Q_W plots for comparison. Although the shape of the plots are roughly the same, there appears to be a major difference in the scaling, indicating that the velocity gradients in *tbl* are considerably lower than in *mega* for the same Reynolds number. The reasons for this difference need to be pursued in future work.

5. Conclusions

In all flow cases considered here, motions with the highest dissipation of kinetic energy per unit volume were of the topological classification stable focus with stretching as found from $Q - R$ plots.

In the case designated as *hipairex*, the flow was initiated from a laminar layer with an error function profile and the maximum Reynolds number R_δ to which the flow evolved was 3000. Here, the highly dissipative motions were usually accompanied by a high enstrophy indicating a vortex sheet-like structure. From Q_S versus R_S plots, the rate of stain tensor for dissipating points had a topology of unstable node saddle-saddle with the rate of strains being of a given ratio and with the vorticity

vector tending to align with the intermediate strain β.

In the case of *tbl*, which was initiated from two turbulent boundary layers placed back to back, the highest local Reynolds number considered was $R_\delta = 9000$. Here, the $-Q_S$ versus Q_W plots indicated no preferred structure for the highly dissipating motions although the $Q - R$ plots indicated a strong preference for stable focus stretching. Also, the Q_S versus R_S plots showed that the highly dissipating motions tend toward $\alpha{:}\beta{:}\gamma = 1 : 1 : -2$. No vorticity alignment checks were made, but it is expected that the vorticity vectors will tend to align with the β axis (cf. Sondergaard *et al.*, 1991).

Comparison of two flows at the same local Reynolds number but with two entirely different initial conditions was made using flow cases designated *mega* and *tbl*. Plots of Q versus R and $-Q_S$ versus Q_W when nondimensionalized appropriately show essentially the same topological structure and scaling from $R_\delta = 5000$ even though *mega* was initiated from a laminar error function profile layer and *tbl* from turbulent boundary layers. Although the shape of the plots are roughly the same, there appears to be a major difference in the scaling, indicating that the velocity gradients in *tbl* are considerably lower than in *mega* for the same Reynolds number. The reasons for this difference need to be pursued in future work.

Acknowledgements

We would like to acknowledge the invaluable assistance of Drs. Michael Rogers and Robert Moser of NASA-Ames Research Center in obtaining and understanding the data sets upon which this study is based. We would also like to acknowledge support from ONR Grant N00014-90-J-1976, the Center of Turbulence Research, and C.S.I.R.O.

REFERENCES

ASHURST, W. T., KERSTEIN, A. R., KERR, R. M., & GIBSON, C. H. 1987 Alignment of vorticity and scalar gradients with strain rate in simulated Navier-Stokes turbulence. *Physics of Fluids.* **30,** 2343.

BRADSHAW, P. B. & FERRISS, D. H. 1967 *The Spectral Energy Balance in a Turbulent Mixing Layer.* Aero Res. Council Current Paper No. 899.

CHEN, J. 1991 *The Effect of Compressibility on Conserved Scalar Entrainment in a Plane Free Shear Layer.* Eighth Symposium on Turbulent Shear Flows, Munich K-1, 1-6.

CHEN, J. H., CHONG, M. S., SORIA, J., SONDERGAARD, R., PERRY, A. E., ROGERS, M., MOSER, R., & CANTWELL, B. J. 1990 *A study of the topology of dissipating motions in direct numerical simulations of time-developing compressible and incompressible mixing layers.* Center for Turbulence Research Report CTR-S90.

CHONG, M. S., PERRY, A. E., & CANTWELL, B. J. 1990 A general classification of three-dimensional flow fields. *Physics of Fluids.* **A.2(5),** 765–777.

MOSER, R. & ROGERS, M. 1990 *Mixing transition and the cascade to small scales in a plane mixing layer.* IUTAM Symposium on Stirring and Mixing, La Jolla, CA 20-24 August 1990.

ROGERS, M. & MOSER, R. 1992 The three-dimensional evolution of a plane mixing layer: The Kelvin-Helmholtz Rollup. *J. Fluid Mech, To appear.*

SONDERGAARD, R., CHEN, J., SORIA, J., & CANTWELL, B. 1991 *Local topology of small scale motions in turbulent shear flows.* Eighth Symposium on Turbulent Shear Flows, Munich K-1, 1-6.

SPALART, P. R. 1988 Direct simulation of a turbulent boundary layer up to $R_\theta =$ 1410. *J. Fluid Mech.* **187,** 61–98.